

## MIT Open Access Articles

*Experimental characterization and elementary reaction modeling of solid oxide electrolyte direct carbon fuel cell*

The MIT Faculty has made this article openly available. **Please share** how this access benefits you. Your story matters.

**Citation:** Yu, Xiankai, Yixiang Shi, Hongjian Wang, Ningsheng Cai, Chen Li, Rumen I. Tomov, Jeffrey Hanna, Bartek A. Glowacki, and Ahmed F. Ghoniem. "Experimental Characterization and Elementary Reaction Modeling of Solid Oxide Electrolyte Direct Carbon Fuel Cell." *Journal of Power Sources* 243 (December 2013): 159–171.

**As Published:** <http://dx.doi.org/10.1016/j.jpowsour.2013.05.149>

**Publisher:** Elsevier

**Persistent URL:** <http://hdl.handle.net/1721.1/105391>

**Version:** Author's final manuscript: final author's manuscript post peer review, without publisher's formatting or copy editing

**Terms of use:** Creative Commons Attribution-NonCommercial-NoDerivs License



# **Experimental Characterization and Elementary Reaction**

## **Modeling of Solid Oxide Electrolyte Direct Carbon Fuel Cell**

**Xiankai Yu<sup>a</sup>, Yixiang Shi<sup>a,\*</sup>, Hongjian Wang<sup>a</sup>, Ningsheng Cai<sup>a</sup>, Chen Li<sup>b</sup>, Rumen I.**

**Tomov<sup>d</sup>, Jeffrey Hanna<sup>c</sup>, Bartek A. Glowacki<sup>d</sup> and Ahmed F. Ghoniem<sup>c</sup>,**

a. Key laboratory for Thermal Science and Power Engineering of Ministry of Education,

Tsinghua University, Beijing 100084, China

b. Huaneng Clean Energy Research Institute, Beijing 100098, China

c. Department of Mechanical Engineering, Massachusetts Institute of Technology,

Cambridge, MA 02139, United States

d. Department of Materials Science and Metallurgy, University of Cambridge, Pembroke

Street, Cambridge, CB2 3QZ, United Kingdom

Department of Physics and Energy, University of Limerick, Castletroy, Ireland

Institute of Power Engineering, ul. Augustowka 36, 02-981 Warsaw, Poland

### **Abstract**

A detailed mechanistic model for solid oxide electrolyte direct carbon fuel cell (SO-DCFC) is developed while considering the thermo-chemical and electrochemical elementary reactions in both the carbon bed and the SOFC, as well as the meso-scale transport processes within the carbon bed and the SOFC electrode porous structures. The model is validated using data from a fixed bed carbon gasification experiment and the SO-DCFC performance testing experiments carried out using different carrier gases and

---

\* Corresponding author. Tel.: +86-10-62789955; Fax: +86-10-62770209.

Email: shyx@tsinghua.edu.cn.

at various temperatures. The analyses of the experimental and modeling results indicate the strong influence of the carrier gas on the cell performance. The coupling between carbon gasification and electrochemical oxidation on the SO-DCFC performance that results in an unusual transition zone in the cell polarization curve was predicted by the model, and analyzed in detail at the elementary reaction level. We conclude that the carbon bed physical properties such as the bed height, char conversion ratio and fuel utilization, as well as the temperature significantly limit the performance of the SO-DCFC.

**Key words:** solid oxide electrolyte; direct carbon fuel cell; elementary reaction; modeling; heterogeneous chemistry

## 1. Introduction

Direct carbon fuel cells (DCFCs) have been examined both theoretically and experimentally recently by in a number of research centers and laboratories because of their potential as power sources in portable and stationary systems. DCFCs are generally divided into two main categories [1, 2]: (1) Direct carbon fuel cells based on high temperature, solid oxide electrolyte fuel cells (SOFCs), using a molten metal (tin) at the anode, also known as liquid tin anode SOFCs (LTA-SOFC); (2) direct carbon fuel cells based on high temperature, solid oxide electrolyte fuel cells (SO-DCFC) or molten carbonate fuel cells (MCFCs), using a mixture of molten carbonates at the anode.

This work is focuses on the solid oxide electrolyte direct carbon fuel cells (SO-DCFC) which are capable of conversing chemical energy in the solid carbon fuel into electricity. These offer a number of advantages over the traditional carbon conversion technologies

as well as alternative DCFCs such as: the abundance of the fuel source, high theoretical efficiency, high CO<sub>2</sub> emission reduction potential, relatively higher reaction activity ascribed to its high operating temperatures, and avoidance of liquid electrolyte consumption, leakage and corrosion [3]. Due to these advantages, some researchers have investigated DFFCs for application in large-scale power plants [4, 5] considering their potential merits for high efficiency and emission reduction.

SO-DCFC performance improvement relies on optimal electrochemical reactions, carbon gasification and mass transport processes. Since experimental studies on SO-DCFC are rather complex, expensive, and time-consuming, comprehensive mathematical models are essential for the technology development. A validated mechanistic model would offer means to gain insight into the complex physical phenomena governing the fuel cell performance that is not readily accessible experimentally, and it can also be useful tool for cell design and operating condition optimization.

Modeling and experimental studies of SO-DCFCs have been reported recently by several researchers [6-9]. Numerous SOFC models considering the intricate interdependency among ionic and electronic conduction, gas transport phenomena, and electrochemical processes have been reported in the literatures for pure hydrogen, syngas or methane [10-20]. Hecht et al. [21] further reported a multi-step heterogeneous elementary reaction mechanism for CH<sub>4</sub> reforming using Ni as catalyst. Janardhanan et al. [22] developed an extended version of the mechanism evaluated for temperatures between 220°C and 1700°C. We also developed a transient elementary reaction model coupled with anodic elementary heterogeneous reactions (adsorption/desorption and water-gas-shift reactions) and electrochemical kinetics for syngas operation (mixtures of

H<sub>2</sub>, H<sub>2</sub>O, CO, CO<sub>2</sub> and N<sub>2</sub>) based on an anode supported button cell [3]. For the full DCFC modeling, Liu et al [23] developed a comprehensive model of molten carbonate DCFC (MC-DCFC) by considering global electrochemical kinetics, mass and charge balance. Li et al. [24] further improved this model, and took into consideration both the anodic electrochemical reaction mechanism and the effects of carbon fuel microstructures. The anodic reaction mechanisms with carbon black and graphite fuels were discussed further.

Zhao et al. [25] developed the SO-DCFC model with carbon fuel from CH<sub>4</sub> cracking. The model considered the global carbon gasification reactions, and analyzed the effect of exchange current density and the anodic CO diffusion coefficients on the cell performance. However, the simulation results were not experimentally validated, and the detailed carbon gasification kinetics and the diffusion processes within the carbon bed were not considered.

From the discussions above, it is clear that most of the kinetic modeling studies on SO-DCFCs have focused on the fuel cell reaction kinetics, while detailed mechanistic models coupling the carbon fuel bed and fuel cell reactions and transport processes are rarely reported. In order to obtain the requisite insight into this coupling and to enable the optimization of the overall performance of the fuel cell system, it is essential to develop a combined mechanistic model based on the carbon gasification mechanism and the SOFCs anode mechanism. Furthermore, for a given mathematical model, most of the model parameters are determined from previous experiments or from the literature, some are adjusted to ensure good agreement between the model results and the new

experimental data. In order to ensure model reliability, both comprehensive experimental tests and model validations are needed.

In this paper, a comprehensive elementary reaction mechanism for the SO-DCFC is developed by coupling the electrochemical reactions, charge transport and mass transport processes within the SOFC and the thermo-chemistry of the carbon bed. The model is validated using experimental data obtained for simple carbon bed gasification setup as well as for the SO-DCFC testing setup with different anode carrier gases and at various carbon bed temperatures. The effects of the operating temperatures, carrier gas composition and carbon bed properties on the SO-DCFC performances are systematically investigated.

## **2. Experiment**

### **2.1 SOFC button cell structure and fabrication**

A Ni/Yttria-stabilized zirconia (YSZ) cermet electrode was used in SOFC button cells that were fabricated by the Shanghai Institute of Ceramics, Chinese Academy of Sciences (SICCAS) [26]. It consisted of a Ni/YSZ anode support layer (680 $\mu\text{m}$ ), a Ni/ScSZ anode active interlayer (15 $\mu\text{m}$ ), a ScSZ electrolyte layer (20 $\mu\text{m}$ ), and a lanthanum strontium manganate (LSM)/ScSZ cathode layer (15 $\mu\text{m}$ ). The diameter of the cathode was 1.3 cm and the diameters of all other layers were 2.6 cm. Before testing, silver paste was deposited on the anode and the cathode surfaces by screen-printing for current collection.

### **2.2 DCFC testing setup and apparatus**

The single carbon bed setup is illustrated in Fig. 1 [26]. A quartz tube loaded with carbon fuel is formed as fixed bed and embedded in another quartz tube that is heated in a

furnace keeping stable at the working temperature. CO<sub>2</sub> flows into the tube through the inlet. For more detailed description see ref. [22].

The SO-DCFC system experimental setup plus the carbon bed are shown in Fig. 2 (a) [26]. The button cell is located at the end of two coaxial alumina tubes and is impacted by an alumina plate which is strained by springs. The Pt mesh is used as the cathode current collector and is fixed to the porous cathode with silver paste screen-printed on the surface. The oxidant flows into the inner tube to the cathode and passes through the porous Pt mesh. A Ni felt (thickness 2 mm) is fixed to the anode support layer with silver paste to collect anode current. The carrier gases are introduced to the inlet of the carbon bed which is surrounded by an alumina tube. Due to the porous structure of foamed Ni felt, the anode gases can reach the anode easily. For both the anode and the cathode, Pt wires are used as voltage and current probes. A glass ring is used as sealant to separate the anode gas and cathode gas. The impacted alumina plate with a through-hole of the same diameter of the cell cathode is used to strain the carbon bed. The layout of the carbon bed is exhibited in Fig. 2 (b). A ring Ni felt is used for auxiliary current collection. The carbon bed is loaded in the middle of cell anode and a thick Ni felt at the bottom.

All of the devices are enclosed in one quartz tube and heated by a furnace to the operational temperature. Pure H<sub>2</sub> is passed through the chamber for 1 h to fully reduce the anode at a flow rate of 50 sccm (Standard Cubic Centimeter per Minute). Then, two kinds of carrier gases, with different flow rates and at various temperatures are introduced into the system. All the carbon fuel used is amorphous carbon black (Black Pearls 2000, GP-3848, Cabot Company), the particle diameter of which is ranged in 150 to 200 μm after grinding and screening.

### **Fig. 1 Single carbon bed experimental system for carbon reaction kinetics**

### **Fig. 2 Experimental setup of SO-DCFC system**

#### 2.3 Carbon bed gasification experiments

Fig. 1 describes the carbon gasification experimental setup. Argon carrier gas with flow rate of 100 sccm is used to purge the gas chamber for one hour. The carbon bed is then heated at a rate of  $30^{\circ}\text{C min}^{-1}$  under the inert Ar atmosphere. Next,  $\text{CO}_2$  with flow rate at 40 sccm is introduced into the bed while the bed temperature is kept at 900, 925 or  $950^{\circ}\text{C}$ . The gaseous product compositions are determined using Gas Chromatography. In practice, the gas produced via bed gasification is sampled every 3 minutes. The total mass of the gas is obtained using Simpson Integral Law. The carbon conversion ratio  $X_c$  defined as the net removal of the solid carbon from the bed carbon through gasification is calculated by the following expression:

$$X_c = \frac{m_{\text{CO}}}{2m_0} \quad (1)$$

where  $m_{\text{CO}}$  is the total mass of carbon in CO gas and  $m_0$  stands for the overall mass of initial carbon fuel.

#### 2.4 SO-DCFC performance characterization

The SO-DCFC is experimentally tested in different gaseous atmospheres at various temperatures for the carbon bed and the fuel cell. The cell polarization curves are measured using a four-probe method with an electrochemical workstation (IM6ex, Zahner-GmbH, Germany). The SO-DCFC is kept at OCV condition for 30 minutes before the polarization curve was measured. First, the carbon bed is packed with 50 mg



Black Pearls. CO<sub>2</sub> or Ar gas with different flow rates (40sccm Ar, 0sccm Ar and 40sccm CO<sub>2</sub>) is introduced to the inlet of the carbon bed inlet, and air with flow rate at 100sccm is introduced to the cathode. Polarization curves are measured at 800°C for both the carbon bed and fuel cell. Second, 300 mg Black Pearls are loaded in the carbon bed and the fuel cell setup is heated up to 850°C. 50 sccm CO<sub>2</sub> is flown into the bed and 100 sccm O<sub>2</sub> into the cathode chamber. Then, the polarization curves are obtained at bed temperatures of 800, 850, 900 and 950°C.

### 3. Model development

#### 3.1 Model assumptions and geometry

The following assumptions are made:

- (1) The gases are ideal gases;
- (2) The temperature within the cell and the carbon bed is uniform. All parameters are evaluated at the given temperature;
- (3) The electrochemical mechanism and the carbon gasification mechanism are modeled using a set of elementary reactions that represent chemical reactivity at the molecular scale;
- (4) The charge transfer reactions take place at the three phase boundary (TPB) as
 
$$CO(Ni) + O^{2-}(YSZ) \rightleftharpoons CO_2(Ni) + (YSZ) + 2e^-;$$
- (5) The microstructures of the electrodes are stable and homogeneous during the experiment. The distributions of the two conducting phases (electronic and ionic) in the electrodes are uniform.

A one-dimensional (1D) geometry for SO-DCFC is also assumed for the domains and the boundaries labeled in Fig. 3. A 1D model is developed for the SO-DCFC with the above assumptions and simplified model geometry.

### **Fig. 3 SO-DCFC model calculation domains and boundaries**

## 3.2 Governing equations

### 3.2.1. Carbon gasification mechanism in the carbon bed and the SOFCs anode mechanism

The carbon gasification mechanism used in this paper is summarized and reduced from the reported carbon gasification reaction mechanisms in the published literature [27, 28]. The detailed reaction parameters are shown in table 1.

### **Table 1 Reduced heterogeneous reaction mechanism for carbon gasification and mechanism on the Ni-based catalysts**

A simplified heterogeneous SOFCs anodic reactions mechanism described in the work of Hecht et al. [29], Janardhanan and Deutschmann [30] and Zhu and Kee [31] is applied. Elementary reactions and the corresponding kinetic parameters are also listed in Table 1. The net molar production rate of gaseous or surface species in a heterogeneous reaction and the reaction rate of each elementary reaction can be explained by mass action kinetics formulations as described in detail in our previous studies [26].

### 3.2.2 Equations for the carbon gasification process

The overall carbon gasification reaction is given as  $C + CO_2 = 2CO$ , which can be modeled using a seven elementary reaction mechanism, as showed in Table 1. The

gasification mechanism yields the following expression for the net rate of carbon atom removal from the bulk carbon,  $R_{i,c}$  [32] (in unit of  $\text{kg m}^{-2} \text{s}^{-1}$ ):

$$R_{i,c} = M_c \{k_2[O(C)] + k_3[CO_2][O(C)] + k_{4r}[CO(C)] - k_{4f}[C_f][CO]\} \quad (2)$$

where  $M_c$  is the mole weight of carbon.

The carbon conversion ratio  $x_c$  satisfies the following differential equation [32]:

$$-\frac{1}{m_c} \frac{dm_c}{dt} = \frac{1}{(1-x_c)} \frac{dx_c}{dt} = S_{gC} R_{i,c} \quad (3)$$

$S_{gC}$  is the specific surface area of the char in unit of  $\text{m}^2 \text{kg}^{-1}$  [32]:

$$S_{gC} = S_{gC,0} \sqrt{1 - \psi \ln(1-x_c)} \quad (4)$$

where  $\psi$  is the structural parameter of the solid carbon fuel. The higher the value of  $\psi$ , the greater the micro-porosity of the char. The overall net molar reaction rates of CO and CO<sub>2</sub> according to the mechanism are:

$$R_{CO} = k_{1f}[CO_2][C_f] - k_{1r}[O(C)] + k_2[O(C)] + 2k_3[CO_2][O(C)] - k_{4f}[C_f][CO] + k_{4r}[CO(C)] - k_5[CO(C)][CO] \quad (5)$$

$$R_{CO_2} = -k_{1f}[CO_2][C_f] + k_{1r}[O(C)][CO] - k_3[O(C)][CO_2] + k_5[CO][CO(C)] \quad (6)$$

Adsorbed species concentrations change due to the combined effect of the chemical reaction and the evolution of the surface area of the carbonaceous fuel. Accounting for these changes, the evolution in O(C) and CO(C) concentrations are described in the equations below [28]

$$\frac{d[O(C)]}{dt} = \{k_{1f}[C_f][CO_2] - k_{1r}[CO][O(C)] - k_2[O(C)]\} + A[O(C)]R_{i,c} \quad (7)$$

$$\frac{d[CO(C)]}{dt} = \{k_{4f}[C_f][CO] - k_{4r}[CO(C)] - k_5[CO][CO(C)]\} + A[CO(C)]R_{i,c} \quad (8)$$

where  $A = \frac{S_{gC,0}^2}{S_{gC}} \left( \frac{S_{gC}^2}{S_{gC,0}^2} - \frac{\psi}{2} \right)$ ,  $[C_f] = c_{sites} - [O(C)] - [CO(C)]$

and  $c_{sites}$  is the surface carbon site concentration.

For the carbon bed, the gas phase mass conservation coupled with the Darcy's law gives [33]:

$$\frac{\partial(\rho\varepsilon)}{\partial t} + \nabla \cdot \rho \mathbf{u} = S_{gC} \frac{m_c}{V_{bed}(\varepsilon + (1-\varepsilon)\varepsilon_p)} (M_{CO}R_{CO} + M_{CO_2}R_{CO_2}) \quad (9)$$

$$\mathbf{u} = -\frac{\kappa}{\eta} \nabla P \quad (10)$$

where  $\kappa$  is the permeability of the carbon bed,  $\eta$  is the gas dynamic viscosity and  $\rho$  is the gas density,  $\varepsilon$  and  $\varepsilon_p$  are the bed and carbon particle porosities, respectively.

At the anode surface, the current density is expressed as  $i_{surf}$ . According to the electrochemical reaction, the flux of CO or CO<sub>2</sub> equals to  $i_{surf} / (2F)$ . Thus, the Darcy velocity is:

$$\mathbf{u} \Big|_{z=0} = \frac{i_{surf}}{2F} (M_{CO_2} - M_{CO}) / \rho \quad (11)$$

The transports of CO and CO<sub>2</sub> through the carbon bed are governed by the following convection-diffusion-reaction equation [33]:

$$\frac{\partial(c_i \varepsilon)}{\partial t} + \nabla \cdot (-D_{eff} \nabla c_i + c_i \mathbf{u}) = S_{gc} \frac{m_c}{V_{bed}(\varepsilon + (1-\varepsilon)\varepsilon_p)} R_i \quad (12)$$

$$D_{eff} = \frac{\varepsilon}{\tau_{bed}} D_{CO\_CO2} \quad (13)$$

where  $\tau_{bed}$  is the tortuosity of the carbon bed.

### 3.2.3. Equations for processes in SOFCs

Heterogeneous chemistry (Tabel 2 Eqs. (14) - (19)) at the surface of the fuel cell anode is used. The surface adsorbates are assumed to be uniformly distributed over the Ni surface. The species molar production rates depend on the gaseous species concentration and the surface species concentration, which are expressed by the coverage. The coverage  $\theta_k$  is the fraction of the surface active sites covered by the adsorbed species k. It is assumed that the total number of surface active sites is conserved and the saturation sorbent capacity is described by the maximum surface sites density  $\Gamma$  [34]. The uncovered Ni surface is treated as a dummy surface species.

Theoretical formulation and computational modeling of elementary charge-transfer chemistry have been suggested by different researchers [35–39]. Here, the anode electrochemical reactions were taken from the model of the patterned SOFC anode [40] and validated by the polarization curves and EIS experimental results. CO charge transfer pathway is considered in this study as  $CO(Ni) + O^{2-}(YSZ) \rightleftharpoons CO_2(Ni) + (YSZ) + 2e^-$ .

Table 2 gives the electrode and electrolyte electrochemistry equations from Eq. (20) to Eq. (37) and mass balance equations from Eq. (38) to Eq. (41).

### **Table 2 Summary of model equations for different processes in SO-DCFCs**

#### 3.3 Boundary conditions

According to the operation conditions and model simplifications, the boundary conditions of the charge, mass and momentum balances' partial differential equations are listed in Table 3.

The boundary conditions “insulation” and “continuity” indicate that the partial derivative is zero or the flux of the variables is continuous at the boundary, respectively.  $c_{gas\_in}$  and  $c_{gas\_ca}$  in the table are the molar concentrations of gaseous species at the inlet of the carbon bed and the cathode. “Pressure”  $P_0$  stands for the ambient pressure condition. At the interface of the anode and the carbon bed, the boundary conditions for the surface species are “insulation”, which is different from the gaseous species. This is because there is no surface species out of the anode. In addition, the gaseous species exchange between the carbon bed and the fuel cell anode due to the electrochemical reaction results in the flux at the corresponding interface  $q_{in} = \frac{i_{surf}}{2F}(M_{CO_2} - M_{CO})$ .  $V_{ca}$  is the cell operation voltage in the calculation.

### **Table 3 Boundary conditions**

### 3.4 Model parameters

The charge and mass balance equations from the model development section require the effective reaction area, the TPB area and the TPB length. The parameter  $S_{TPB}$  can be formulated using the percolation theory and the particle coordination number of the binary random packing of spheres [41, 42, 43]. Similar to the calculation of  $S_{TPB}$ , the parameter  $L_{TPB}$  (TPB length) can also be calculated. Table 4 lists the porosity, mean pore diameter,  $S_{TPB}$  and  $S_{Ni}$  in each layer. The material conductivities and other parameters are shown in Table 5 [26, 44, 45, 46].

#### **Table 4 Pore structure parameters in porous electrode**

#### **Table 5 Properties and parameters for model calculation**

### 3.5 Solution method

Model calculations are performed using the finite element commercial software COMSOL MULTIPHYSICS®. The button cell performance is calculated at a given cell voltage. The average current density at a given cell voltage is derived from the local ionic current density in the electrolyte layer. A complete polarization curve is generated by setting different cell voltages.

## **4. Results and discussion**

### 4.1. Model calibration and validation

The mechanistic model of the SOFC operating on gaseous fuels has been validated in our previous work [22]. The predicted and experimental polarization curves for various

CO/CO<sub>2</sub> mixtures at 750/800/850°C were obtained. The predicted polarization curves agree well with the experimental data at 800°C with 10% CO, 90% CO<sub>2</sub> and 40% CO, 60% CO<sub>2</sub>, which are the base cases for model calibration. For more detailed description of the calibration and validation see ref. 22.

Table 1 shows the kinetic data of the seven elementary reactions of the carbon gasification mechanism for the Black Pearls 2000 used in this paper. In order to verify the kinetic data from Lee et al. [32], a single bed carbon gasification experiment was conducted.

**Fig. 4 Char conversion ratio to time at 900/925/950°C both for experiments and simulation**

The experimental and simulation results shown in Fig. 4 indicate that the modeling results (solid lines) agree well with the experimental data. Thus, the carbon gasification mechanism is applicable to the carbon fuel used in this study. In addition, it is clear that the carbon gasification rate increases as the bed temperature is raised.

#### 4.2 The effects of the anode carrier gas on the SO-DCFC performance

Fig. 5 shows the experimental and simulated polarization curves with Ar and CO<sub>2</sub> as carrier gases at different flow rates. The simulation results generally fit the experimental data well, especially for predicting the anomalous curve shape at 0 sccm Ar flow rate (no argon gas input while almost completely argon throughout the carbon bed for the initial condition) at 800°C. Moreover, the corresponding experimental power density of the fuel cell are measured and plotted as function of the current density in Fig. 6.



### **Fig. 5 I-V curves at different anode gaseous conditions**

### **Fig. 6 Experimental power density curves at different anode gaseous conditions**

When the gas at the carbon bed inlet is pure CO<sub>2</sub> flowing at the rate of 40 sccm, the limiting current density is around twice as that in an Ar atmosphere flowing at the same flow rate. The CO<sub>2</sub> rich atmosphere can promote the CO production reaction via the Boudouard reaction, which raises the electrochemical reaction rate. On the other hand, when the anode chamber is flooded with Ar, the cell performance is severely limited, especially when the anode is purged at a high Ar flow rate (e.g. 40sccm in the experiment).

Another interesting phenomenon is that there exists a current density sluggish period (the “S” shaped curve for the 0sccm Ar inlet condition in Fig. 5 and Fig. 8&9) in which the cell current density remains nearly the same while the cell voltage falls. The “S” shaped curve reflects the coupling between the solid carbon gasification reactions and the cell electrochemical reactions at the conditions where the consumption, production and diffusion of CO<sub>2</sub> in the whole system play important roles.

### **Fig. 7 Distributions of CO and CO<sub>2</sub> throughout the SO-DCFC system**

### **Fig. 8 Net production and consumption of CO<sub>2</sub> in the SO-DCFC**

### **Fig. 9 Averaged concentration variation of CO and CO<sub>2</sub> in both carbon bed and fuel cell**

In order to explore this coupling in more detail, Fig. 7, Fig. 8 and Fig. 9 show the modeling results at the same anode conditions: 0scm Ar flows at 800°C. All plots are obtained for the same polarization process as in Fig. 5. Fig. 7 shows that the gradients of CO or CO<sub>2</sub> concentration in the cell anode are much larger than those in the carbon bed, indicating that the CO production rate by carbon gasification reaction is slower than its consumption by the electrochemical oxidation reaction. CO diffuses from the carbon bed where it is produced to the cell anode where it is consumed. Fig. 8 shows that the CO<sub>2</sub> production at the anode and consumption at the carbon fit similar “S” shapes to that of the current density. Fig. 9 shows the gaseous species concentration evolution, also exhibiting the “S” shaped polarization curve.

From 125 s to 225 s, the current density exhibits a transition that corresponds to the “S” shaped part of the polarization curve for zero Ar flow. We call this time period as the “transition zone”. Before the transition zone, that is at lower current, CO accumulated during the heat-up period is quickly consumed by the electrochemical oxidation reaction resulting in a peak of CO<sub>2</sub> concentration in the fuel cell followed by a peak in the carbon bed. The rising dashline shows the delay associated with CO<sub>2</sub> diffusion from the cell to the carbon bed and the difference between CO<sub>2</sub> reaction rates in the carbon bed and the fuel cell. During the transition period, CO<sub>2</sub> concentration in the fuel cell anode begins to drop because of the growing CO<sub>2</sub> diffusion rate and the receding CO<sub>2</sub> production rate, caused by the drop in the CO concentration that limits the electrochemical oxidation reactions. Meanwhile, CO<sub>2</sub> in the carbon bed gradually accumulates, which is shown on the right-hand side of the second (descending) arrow following the transition zone. This analysis demonstrates that the gas transport between the carbon bed and the fuel cell

impacts the cell performance, limiting the fuel supply to the anode at intermediate currents.

Furthermore, according to Fig. 6, the experimental maximum power density is around  $274 \text{ W m}^{-2}$  which occurs in the “transition zone” at 0 sccm Ar primarily due to the coupling between the gasification and electrochemistry via CO-CO<sub>2</sub> transport between the carbon bed and the anode, as described above. The peak power density occurs in the condition of “0 sccm argon” which, however, is followed by a drastic decline in the cell performance as the current increases slightly. Thus, according to the experimental data, it is better to operate with CO<sub>2</sub> as the anode carrier.

#### 4.3 The effects of the carbon bed temperature

The carbon bed temperature has multiple effects on the cell performance. Fig. 10 depicts the experimental and predicted polarization curves at different carbon bed temperatures described in part 2.4 in detail. The modeling results match the experimental data. Both of the experimental and simulated data suggest that, as the carbon bed operational temperature increases, the cell performance improves and the open circuit voltage increases. A higher carbon bed temperature results in higher carbon gasification rate, and thus more CO is produced for the electrochemical reaction. Moreover, it can be seen that the SO-DCFC performance is limited by the relatively low reaction rate of carbon gasification. Although the cell can operate on CO at 800°C, under gasification conditions, the impact of the gas diffusion on polarization results in the low CO concentration at the cell anode.

**Fig. 10 Polarization curves for different carbon bed temperature**

A sensitivity analysis was conducted to evaluate the impact of the gasification elementary reactions on the maximum power density when artificially increasing or reducing the gasification rate by 20 percent. The temperature is fixed at 800°C, and 40 sccm CO<sub>2</sub> flows into the carbon bed. Fig. 11 shows the modeling results, which indicate that the elementary reactions RR.1  $CO_2 + C_f \rightleftharpoons CO + O(C)$  and RR.2  $C_b + O(C) \longrightarrow CO + C_f$  are the primary limiting elementary reaction steps for carbon gasification. Fig. 12 further shows the elementary reaction rates of RR.1 and RR.2 in the carbon bed at 800°C and 900°C, suggesting faster rates for these two elementary reactions at higher temperature. In summary, the results from Fig. 11&12 indicate that the better overall performance of the cell at higher temperature can be ascribed to the higher carbon gasification reaction rates of the two elementary reactions of RR.1 and RR.2.

**Fig. 11 Relative change of  $P_{max}$  for the sensitivity analysis of carbon gasification elementary reactions.**

**Fig. 12 Elementary reaction rates of RR.1 and RR.2 in carbon bed at 800°C and 900°C**

Fig. 13 shows the CO<sub>2</sub> concentration distribution along the carbon bed and the fuel cell anode. Since the CO produced by gasification in the carbon bed diffuses towards both ends – the bed inlet and the fuel cell anode -, the CO concentration plots show convex shapes. The corresponding concave distribution of CO<sub>2</sub> leads to the carbon gasification reaction shown in Fig. 12 for the two key elementary reaction steps RR.1 and RR.2.

**Fig. 13 Concentration distributions of CO<sub>2</sub> and adsorbed oxygen species O(C) at 800°C and 900°C**

Moreover, the surface concentration of adsorbed oxygen species O(C), which is an important intermediate species for carbon gasification in reaction RR.1 and RR.2 is shown in Fig. 13. It is clear that the O(C) surface concentration has the same trend as the two reaction rates, which implies the dominant roles of reaction RR.1 and RR.2 for carbon gasification processes.

#### 4.4 The effects of the fuel cell working voltages and the carbon bed geometry

**Fig. 14 Power density P and carbon utilization  $\eta_{char}$  curves for different cell work voltages**

Fig.14 depicts the modeling results for the cell power density and carbon utilization at different operating voltages (90%, 80%, 60% 50% and 40% of the OCV are selected) at 800°C with 40 sccm CO<sub>2</sub> as the anode carrier gas. Here, the carbon utilization is defined by the following expression:

$$\eta_{char} = \frac{\pi r_0^2 i_{surf} / (4F)}{\int_H \frac{(1/2)R_{CO} \Delta S_{GC}}{H} dx} \quad (43)$$

Where  $r_0$  is the bed radius,  $i_{surf}$  is the current density at the interface between bed and cell anode,  $R_{CO}$  is the net production rate of CO in the carbon bed. The numerator in the expression stands for the equivalent consumption of carbon per unit time purely due to the electrochemical reaction  $CO(Ni) + O^{2-}(YSZ) \rightarrow CO_2(Ni) + (YSZ) + 2e^-$  at the interface of carbon bed and cell anode, while the denominator is the total equivalent carbon

consumption per unit time in carbon bed. Specifically, according to the Boudouard Reaction  $CO_2 + C = 2CO$ , the net rate of carbon consumption equals to half of the net production rate of CO, resulting in the net production of CO per unit bed height and per unit time expressed as  $\frac{(1/2)R_{co}m_{sc}}{H}$ . Thus the total net production rate of CO is obtained by integrating  $\frac{(1/2)R_{co}m_{sc}}{H}$  along the carbon bed height showed as the denominator in the expression of carbon utilization above.

Fig.14 indicates that when the cell voltage is lower, at around 60% of OCV, the output power density P is close to the maximum value. Moreover, the effect of the intrinsic carbon bed properties, such as the carbon conversion and the carbon utilization (averaged over the carbon bed) on the performance are also important. Fig. 15 reveals the relationship between the carbon conversion and carbon utilization. It shows that the carbon utilization stays almost the same while the conversion increases up to 0.65 and then sharply rises resulting mainly from the fast consumption of the carbon bed. Analyzing the data presented in Fig. 14 and Fig. 15, we conclude that the optimized working condition for the SO-DCFC is 60% of OCV, corresponding to an averaged carbon conversion of 0.65, which is the limit before the carbon bed replinshed. This operating condition ensures that the fuel cell is at a relatively stable working environment with a steady power density of about  $190W m^{-2}$  and carbon utilization of some 30% and at a relatively high output voltage of 60% OCV.

**Fig. 15 The relationship between carbon utilization  $\eta_{char}$  and conversion  $X_c$**

The carbon bed height is another key parameter, when the radius of the bed is fixed at the same value as the cell cathode. The working voltage of fuel cell is set to 60% of the OCV, which is the optimized condition described above, while the bed height is arranged between 0.001m to 0.1m, as illustrated in Fig. 16.

### **Fig. 16 Power density and carbon utilization degree for different carbon bed heights**

Fig. 16 shows that a higher carbon bed height ensures higher carbon utilization, and improves the power density. However, it should be noted that these two parameters do not continue to increase beyond a certain bed height (e.g. larger than 0.1 m for the present conditions). In fact, the cell performance is limited by both the carbon bed height and the carbon utilization. With increasing of the bed height, more CO is supplied to the anode hence raising the power density. When the carbon bed is high enough, the cell performance is not be limited by the CO production rate anymore but mainly by the electrochemical reaction rate. At the same time, the carbon utilization basically stays constant or even falls down.

## **5. Conclusion**

A mechanistic SO-DCFC model is developed by considering the thermochemical and electrochemical elementary reactions in both the carbon bed and the SOFC, as well as the transport processes within carbon bed and within SOFC electrode porous structures. The model is validated using the data from both fixed bed carbon gasification experiments and the SO-DCFC performance tests carried out with different carrier gases and at various temperatures. The analyses of the experimental and the modeling results show the

strong influence of the carrier gases on the cell performance. Namely, a higher CO<sub>2</sub> flow rate at the carbon bed inlet contributes to a better cell performance with the maximum power density of nearly 213 W m<sup>-2</sup> at temperature of 800°C. On the other hand, higher argon flow rate results in worse cell performance with the maximum power density of nearly 274 W m<sup>-2</sup> at the same temperature.

The coupling of the carbon fuel gasification and the electrochemical oxidation on the SO-DCFC performance which result in a transition zone of the cell polarization curve was predicted and analyzed at the elementary reaction level. The elementary reactions of RR.1 and RR.2 are found to be of key importance for the carbon gasification process. According to the numerical simulation, higher temperature leads to faster reaction rates of the two key elementary reactions RR.1 and RR.2 providing more CO for the electrochemical reaction in the anode. As a consequence, higher bed temperature enables better cell performance.

In addition, it is shown that the carbon bed physical properties such as bed height, char conversion as well as the temperature are closely related to the cell performance. Higher carbon bed height benefits the output power density and ensures larger carbon utilization until it reaches a saturation value (e.g. 0.1m for the current simulative situation).

## **Acknowledgements**

This work was supported by the National Natural Science Foundation of China (20776078, 51106085) and the Seed Funding of Low Carbon Energy University Alliance. We gratefully acknowledge the insightful discussions with Prof. Shaorong Wang in the



Shanghai Institute of Ceramics Chinese Academy of Sciences (SICCAS), China and Dr. Turgut M. Gür in Stanford University.

## **Nomenclature**

## **References**

- [1] D. Rastler, Program on Technology Innovation: Systems Assessment of Direct Carbon Fuel Cells Technology, Electric Power Research Institute (EPRI), (2008) No. 1016170.
- [2] T. P. Chen, D. Rastler, Systems Assessment of Direct Carbon Fuel Cells Technology, Fuel Cell Seminar and Exposition, Phoenix, AZ, (2008) 1246-1251.
- [3] C. Li, Y. Shi, N. Cai, J. Power Sources, 196 (2011) 754-763.
- [4] M. Gazzani, M.C. Romano, J. Eng. Gas Turbines Power 135(1) (2012), 011701.
- [5] M. Li, A.D. Rao, G. S. Samuelsen, Applied Energy, 91 (2012) 43–50.
- [6] J. Mizusaki, H. Tagawa, Solid State Ionics, (1992) 126–134.
- [7] G.O. Lauvstad, R. Tunold, S. Sunde, J. Electrochem. Soc., 149 (12) (2002) E497–E505.
- [8] V. Yurkiv, D. Starukhin, H. R. Volpp, W. G. Bessler, J. Electrochem. Soc., 158 (2011) B5–B10.
- [9] C.J. Moyer, N.P. Sullivan, H. Zhu, R.J. Kee, J. Electrochem. Soc., 158 (2011) B117–B131.
- [10] Y. Shi, N. Cai, C. Li, C. Bao, E. Croiset, J. Qian, Q. Hu, S. Wang, J. Power Sources, 172 (2007) 235-245.
- [11] Y. Shi, N. Cai, C. Li, C. Bao, E. Croiset, J. Qian, Q. Hu, S. Wang, J. Power Sources, 172 (2007) 246-252.
- [12] Y. Shi, N. Cai, C. Li, J. Power Sources, 164 (2007) 639-648.
- [13] K.P. Recknagle, R.E. Williford, L.A. Chick, D.R. Rector, M.A. Khaleel, J. Power Sources, 113 (2003) 109-114.
- [14] H. Yakabe, T. Sakurai, Solid State Ionics, 174 (2004) 295-302.

- [15] N. Autissier, D. Larrain, J. Van herle, D. Favrat, J. Power Sources, 131 (2004) 313-319.
- [16] T. Nishino, H. Iwai, K. Suzuki, J. Fuel Cell Sci. Technol., 3 (2006) 33-44.
- [17] J. Yuan, B. Sunden, J. Fuel Cell Sci. Technol., 3 (2006) 89-98.
- [18] R. Suwanwarangkul, E. Croiset, E. Entchev, S. Charojrochkul, M.D. Pritzker, M.W. Fowler, P.L. Douglas, S. Chewathanakup, H. Mahaudom, J. Power Sources, 161 (2006) 308-322.
- [19] T. Aloui, K. Halouani, Appl. Therm. Eng., 27 (2007) 731-737.
- [20] R.S. Gemmen, J. Trembly, J. Power Sources, 161 (2006) 1084-1095.
- [21] E.S. Hecht, G.K. Gupta, H. Zhu, A.M. Dean, R.J. Kee, L. Maier, O. Deutschmann, Appl. Catal. A 295 (2005) 40-51.
- [22] V.M. Janardhanan, O. Deutschmann, J. Power Sources, 162 (2006) 1192-1202.
- [23] Q. Liu, Y. Tian, C. Xia, J. Power Sources, 185(2008) 1022-1029.
- [24] H. Li, Q. Liu, Y. Li, Electrochimica. Acta, 55(2010) 1958-1965.
- [25] X. Zhao, Q. Yao, S. Li, N. Cai, J. Power Sources, 185(2008) 104-111.
- [26] Y. Shi, C. Li, N. Cai, J. Power Sources, 196 (2011) 5526–5537.
- [27] J. D. Blackwood, A. J. Ingeme, Aust. J. Chem., 13 (1960) 194-209.
- [28] L.Q. Ma, *“Combustion and gasification of chars in oxygen and carbon dioxide at elevated pressure”*, ProQuest Dissertations and Theses, Dissertations & Theses @ Stanford University, pg. n/a (2006).
- [29] E.S. Hecht, G.K. Gupta, H. Zhu, A.M. Dean, R.J. Kee, L. Maier, O. Deutschmann, Appl. Catal. A 295 (2005) 40–51.
- [30] V.M. Janardhanan, O. Deutschmann, J. Power Sources, 162 (2006) 1192–1202.
- [31] H. Zhu, R.J. Kee, J. Electrochem. Soc., 153 (2006) A1765–A1772.
- [32] A. C. Lee, R. E. Mitchell, T. M. Gür, AIChE J., 55 (2009) 983–992.
- [33] B.R. Alexander, R.E. Mitchell, T.M. Gür, J. Electrochem. Soc., 159 (2012) B347-B354.

- [34] R.J. Kee, M.E. Coltrin, P. Blarborg, *Chemically Reacting Flow*, John Wiley & Sons Inc., Hoboken, NJ, 2003.
- [35] W.G. Bessler, S. Gewies, M. Vogler, *Electrochim. Acta*, 53 (2007) 1782–1800.
- [36] H. Zhu, R.J. Kee, V.M. Janardhanan, O. Deutschmann, D.G. Goodwin, *J. Electrochem. Soc.*, 152 (2005) A2427–A2440.
- [37] H. Zhu, R.J. Kee, *J. Electrochem. Soc.*, 155 (2008) B715–B729.
- [38] D.G. Goodwin, H. Zhu, A.M. Colclasure, R.J. Kee, *J. Electrochem. Soc.*, 156 (2009) B1004–B1021.
- [39] W.G. Bessler, J. Warnatz, D.G. Goodwin, *Solid State Ionics*, 177 (2007) 3371–3383.
- [40] Y. Shi, W. Lee, A. Ghoniem, *Fuel Cell*, (2010)33205.
- [41] P. Costamagna, P. Costa, V. Antonucci, *Electrochim. Acta*, 43 (1998) 375–394.
- [42] S.H. Chan, Z.T. Xia, *J. Electrochem. Soc.*, 148 (2001) A388–A394.
- [43] R.J. Kee, M.E. Coltrin, P. Blarborg, *Chemically reacting flow*, John Wiley & Sons. Inc, Hoboken, New Jersey, 2003.
- [44] J. Divisek, R. Wilkenhoner, Y. Volfkovich, *J. Appl. Electrochem.*, 29 (1999) 153–163.
- [45] A. Mitterdorfer, L.J. Gauckler, *Solid State Ionics*, 117 (1999) 203–217.
- [46] P. Costamagna, P. Costa, V. Antonucci, *Electrochim. Acta*, 43 (1998) 375–394.
- [47] A. Bieberle, L.J. Cauckler, *Solid State Ionics* 146 (2002) 23–41.
- [48] Y.X. Shi, N.S. Cai, C. Li, C. Bao, E. Croiset, J.Q. Qian, Q. Hu, S.R. Wang, *J. Electrochem. Soc.* 155 (2008) B270–B280.
- [49] E.A. Mason, A.P. Malinauskas, *Gas Transport in Porous Media: The Dusty-Gas Model*, Elsevier, New York, 1983.
- [50] S. Nagata, A. Momma, T. Kato, Y. Kasuga, Numerical analysis of output characteristics of tubular SOFC with internal reformer, *J. Power Sources* 101 (2001) 60–71.
- [51] R. Suwanwarangkul, E. Croiset, M.W. Fowler, P.L. Douglas, E. Entchev, M.A. Douglas, *J. Power Sources* 122 (2003) 9–18.

- [52] R.J. Braun, Optimal design and operation of solid oxide fuel cell systems for small-scale stationary applications, Ph.D. thesis, University of Wisconsin, Madison, USA, 2002, PP.109-111.
- [53] M. Vogler, A. Bieberle, L. Gauckler, J. Warnatz, W.G. Bessler, J. Electrochem. Soc., (2009) 156(5) B663-72.
- [54] J.H. Nam, D.H. Jeon, J. Electrochim. Acta., 51 (2006) 3446–3460.

## **List of Tables**

**Table 1 Reduced heterogeneous reaction mechanism for carbon gasification and mechanism on the Ni-based catalysts**

**Table 2 Summary of model equations for different processes in SO-DCFCs**

**Table 3 Boundary conditions**

**Table 4 Pore structure parameters in porous electrode**

**Table 5 Properties and parameters for model calculation**

## List of Figures

**Fig. 1** Single carbon bed experimental system for carbon reaction kinetics

**Fig. 2** experimental setup of SO-DCFCs system

**Fig. 3** SO-DCFCs model calculation domains and boundaries

**Fig. 4** Char conversion ratio to time at 900/925/950°C both for experiments and simulation

**Fig. 5** I-V curves at different anode gaseous conditions

**Fig. 6** Experimental power density curves at different anode gaseous conditions

**Fig. 7** Distributions of CO and CO<sub>2</sub> throughout the SO-DCFCs system

**Fig. 8** Net production and consumption of CO<sub>2</sub> in the SO-DCFCs

**Fig. 9** Averaged concentration variation of CO and CO<sub>2</sub> in both carbon bed and fuel cell

**Fig. 10** Polarization curves for different carbon bed temperature

**Fig. 11** Relative change of  $P_{max}$  for the sensitivity analysis of carbon gasification elementary reactions.

**Fig. 12** Elementary reaction rates of RR.1 and RR.2 in carbon bed at 800°C and 900°C

**Fig. 13** Concentration distributions of CO<sub>2</sub> and adsorbed oxygen species O(C) at 800°C and 900°C

**Fig. 14** Power density P and carbon utilization  $\eta_{char}$  curves for different cell work voltages

**Fig. 15** The relationship between carbon utilization  $\eta_{char}$  and conversion  $X_c$

**Fig. 16** Power density and carbon utilization degree for different carbon bed heights



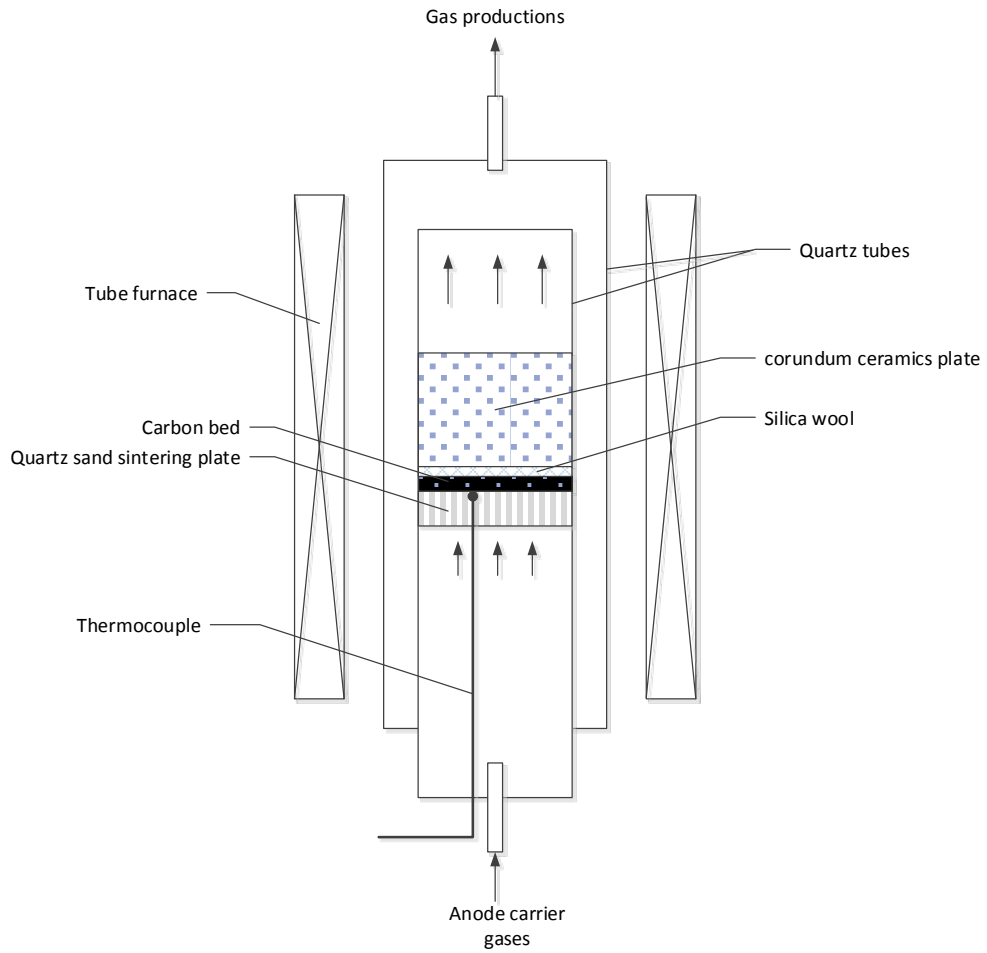
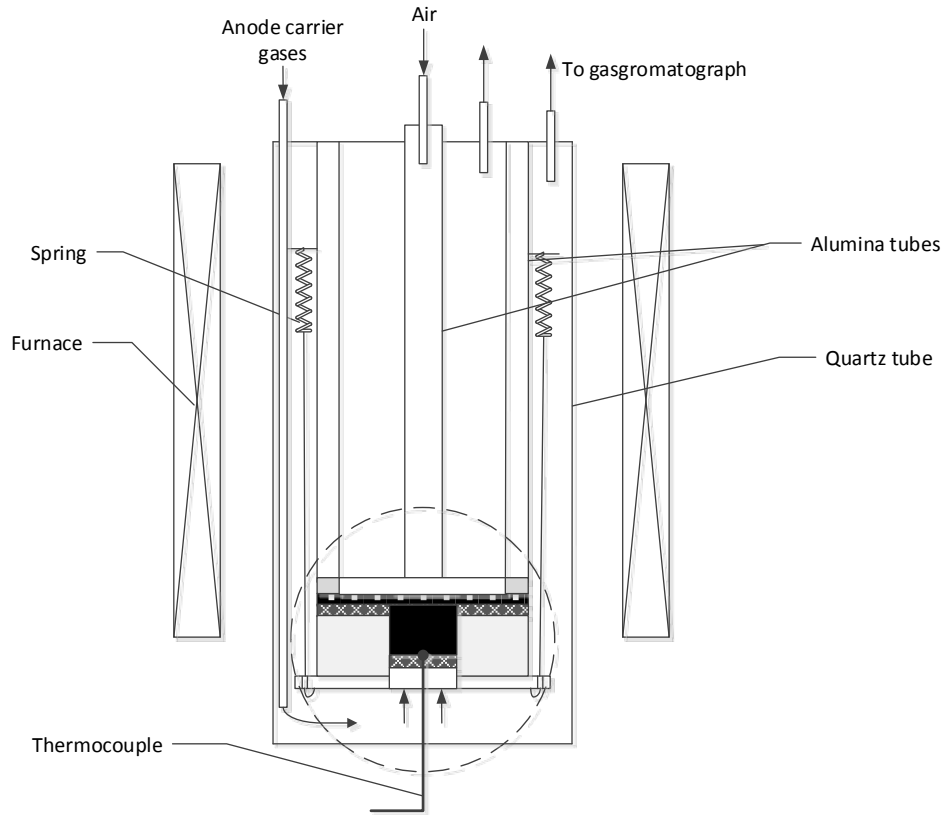
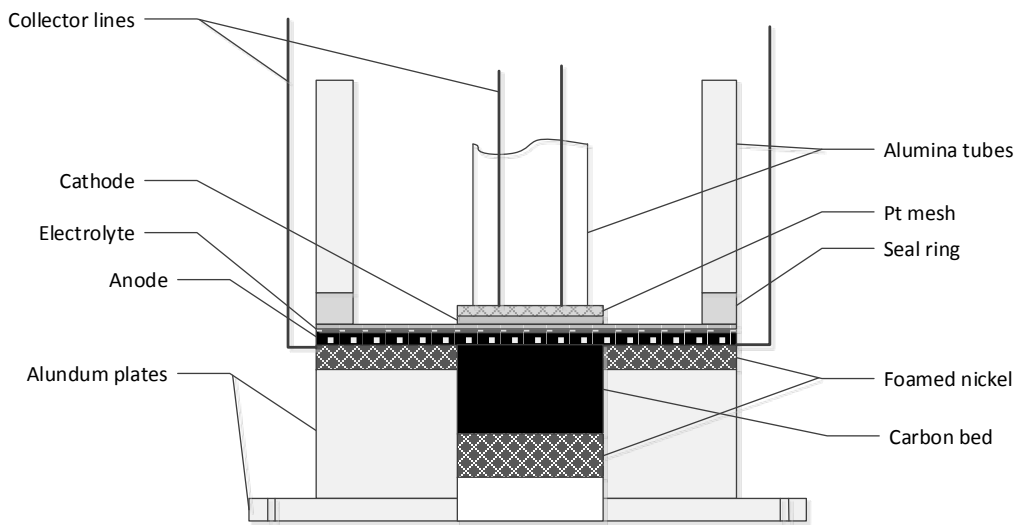


**Fig. 1** Single carbon bed experimental system for carbon reaction kinetics





(a)



(b)

**Fig. 2 Experimental setup of SO-DCFC system**

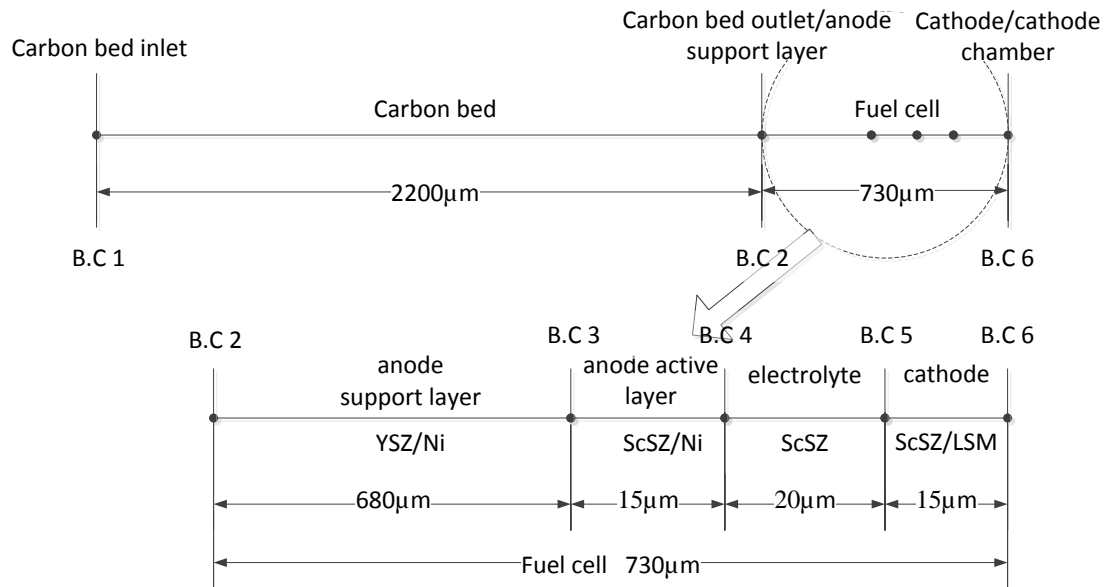


**Fig. 3 SO-DCFC model calculation domains and boundaries**

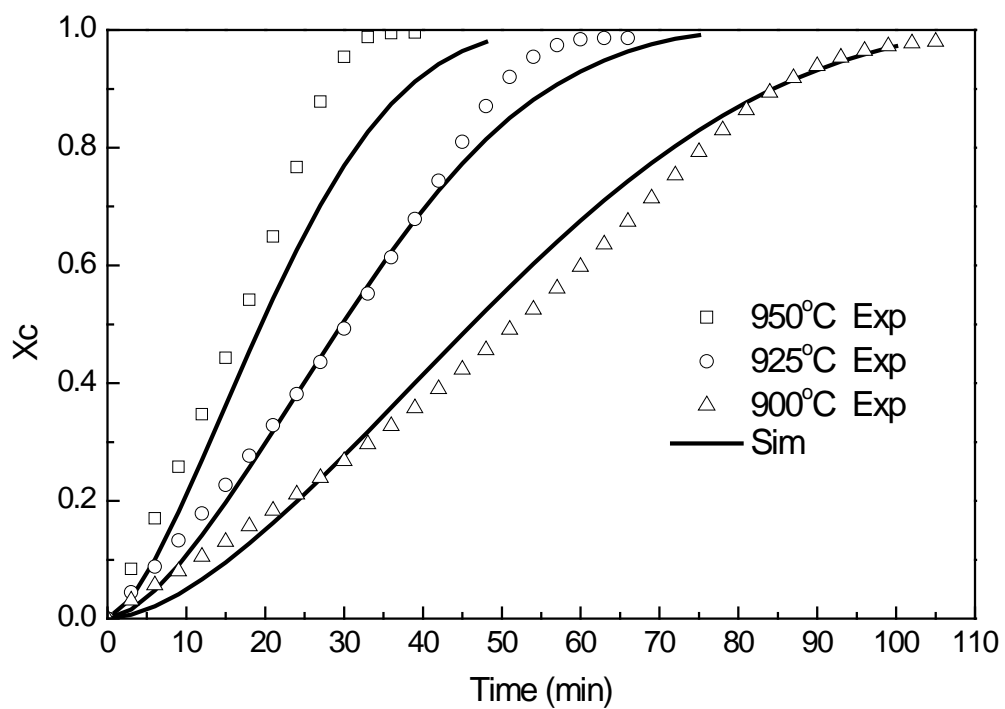


**Fig.**

**4 Char conversion ratio to time at 900/925/950°C both for experiments and simulation**

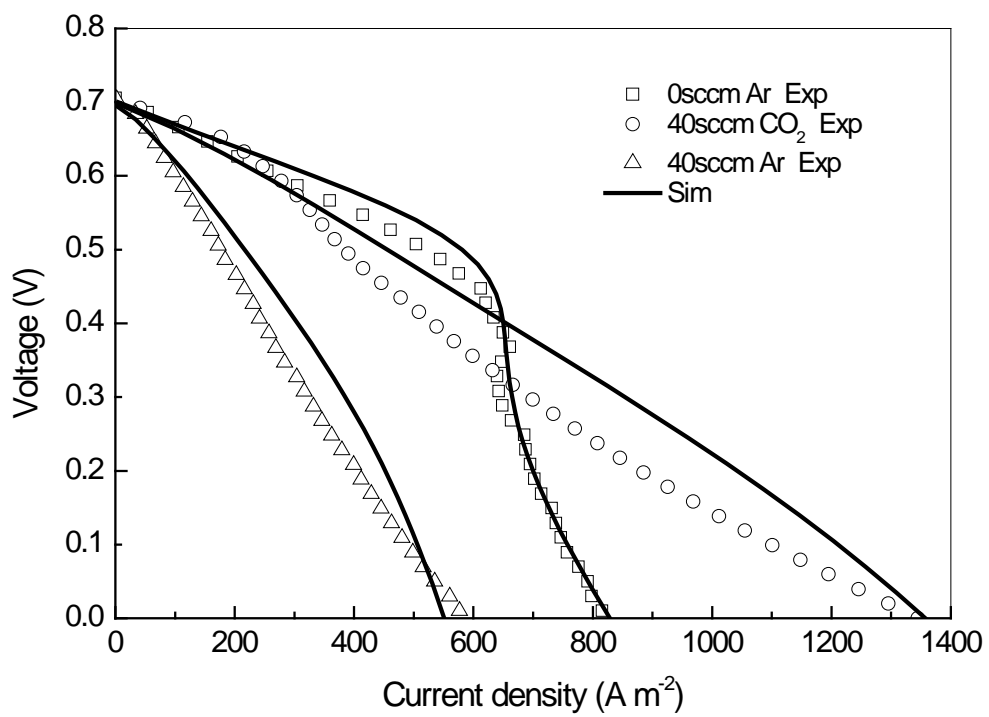


**Fig. 5 I-V curves at different anode gaseous conditions**

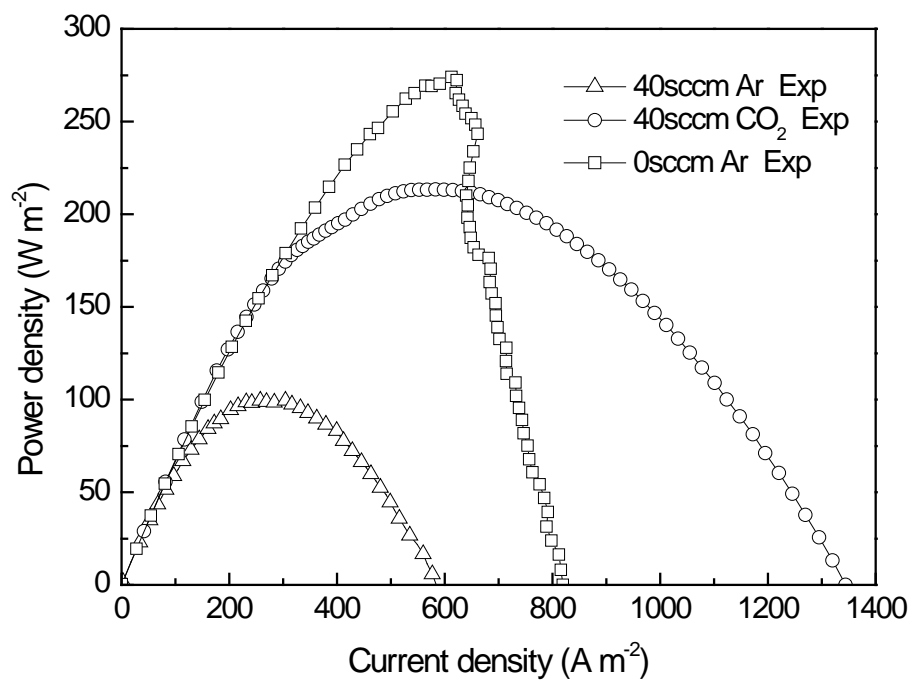


**Fig.**

**6 Experimental power density curves at different anode gaseous conditions**

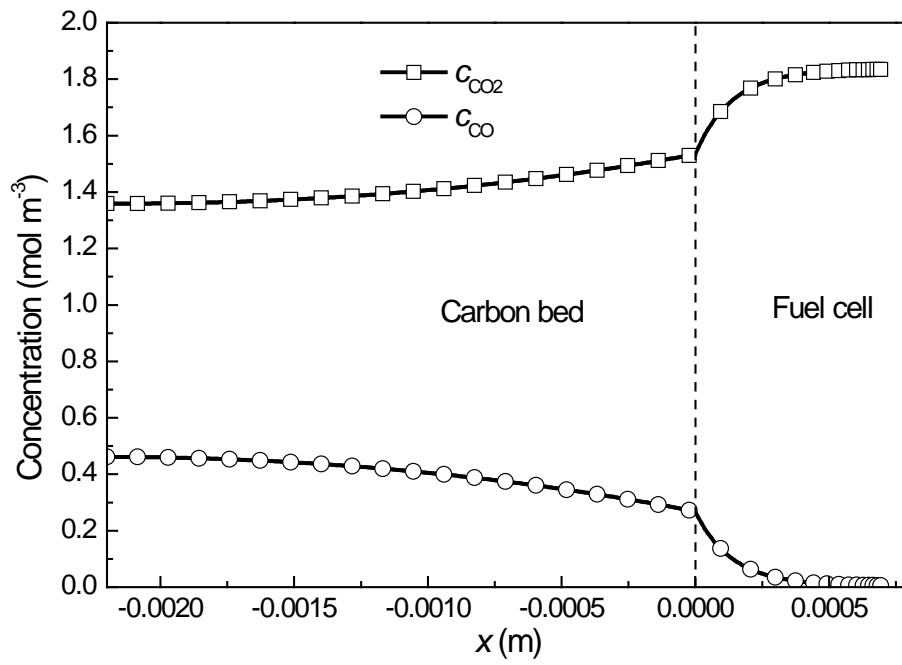


**Fig. 7 Distributions of CO and CO<sub>2</sub> throughout the SO-DCFC system**

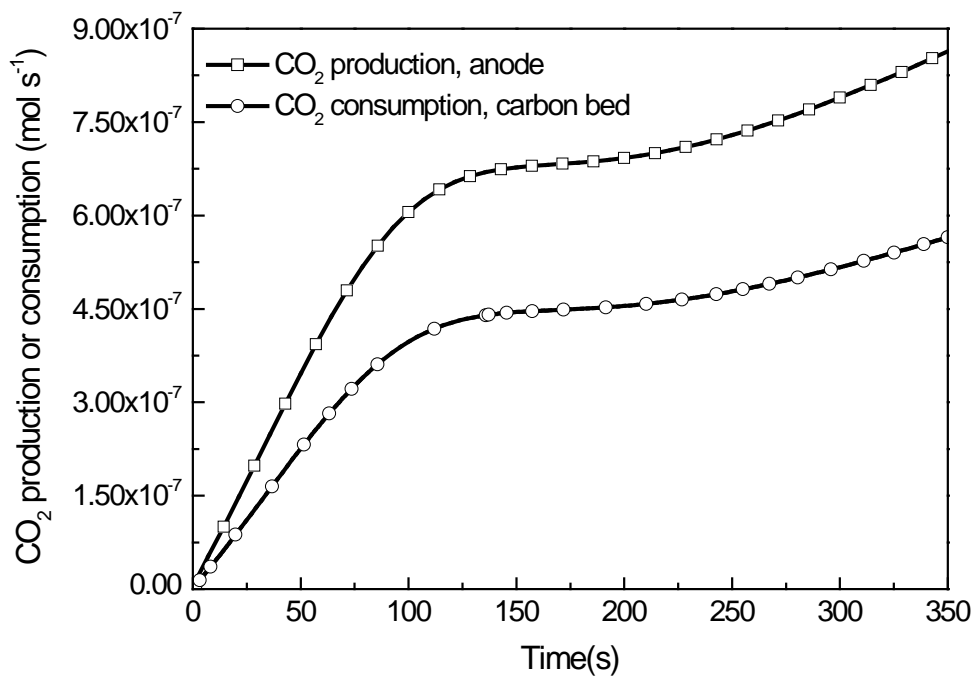


**Fig.**

**8 Net production and consumption of CO<sub>2</sub> in the SO-DCFC**

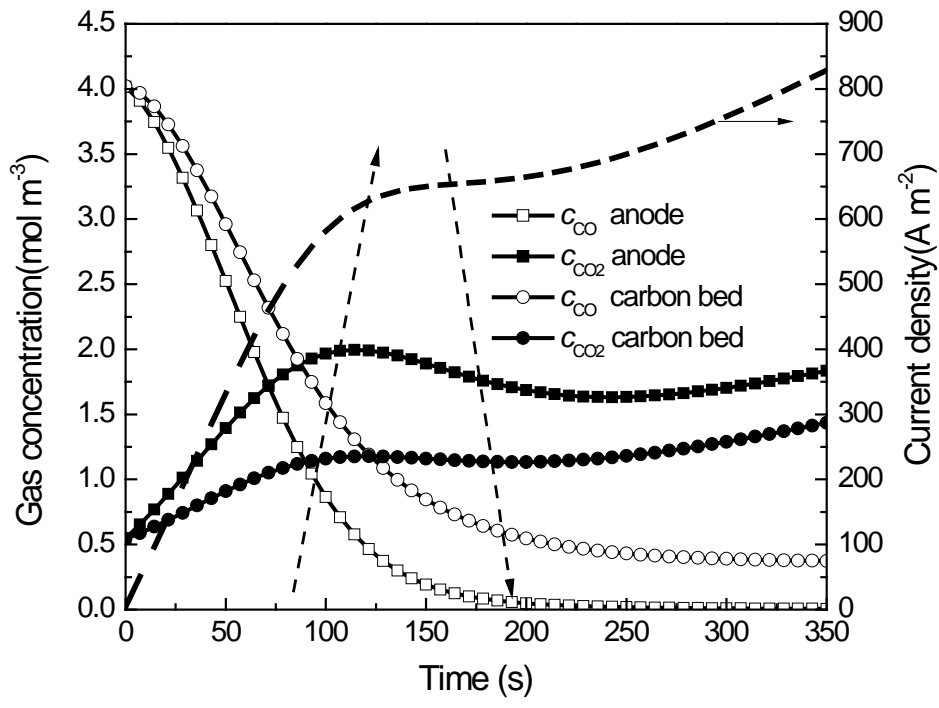


**Fig. 9** Averaged concentration variation of CO and CO<sub>2</sub> in both carbon bed and fuel cell



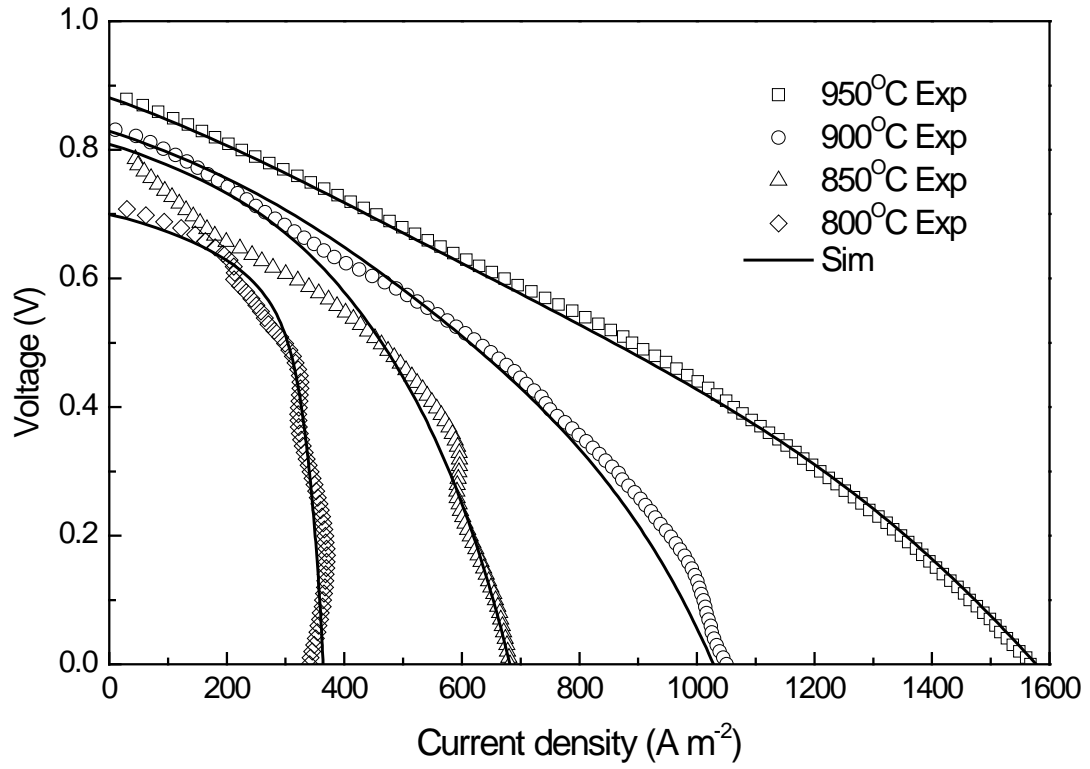
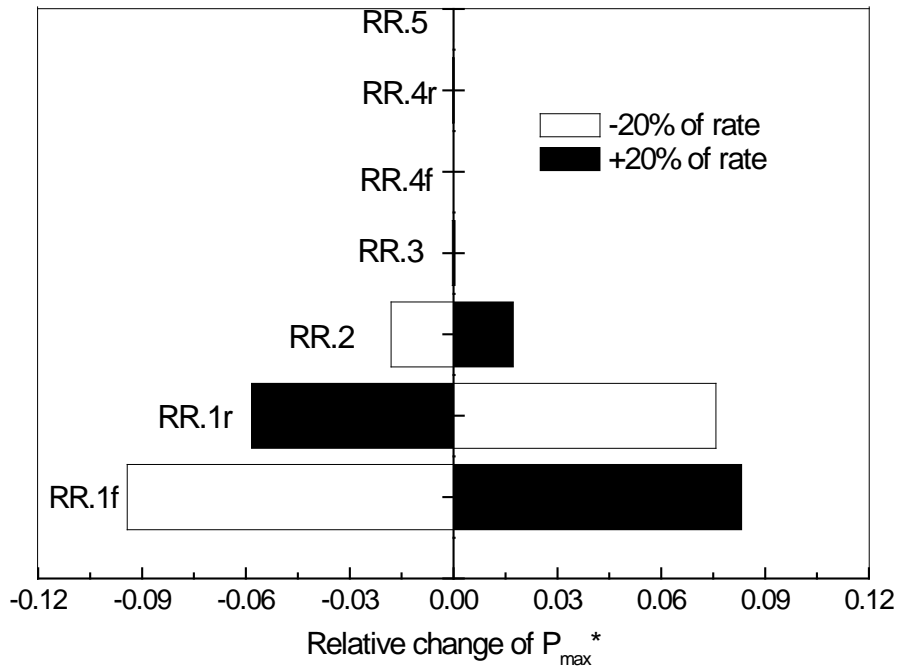


**Fig. 10 Polarization curves for different carbon bed temperature**



\* The

relative change of  $P_{\max}$  is expressed as:  $(P_{\max} - P_0) / P_0$  where  $P_0$  is the maximum power density without changing the elementary reaction rates artificially

**Fig. 11 Relative change of  $P_{\max}$  for the sensitivity analysis of carbon gasification elementary reactions.**

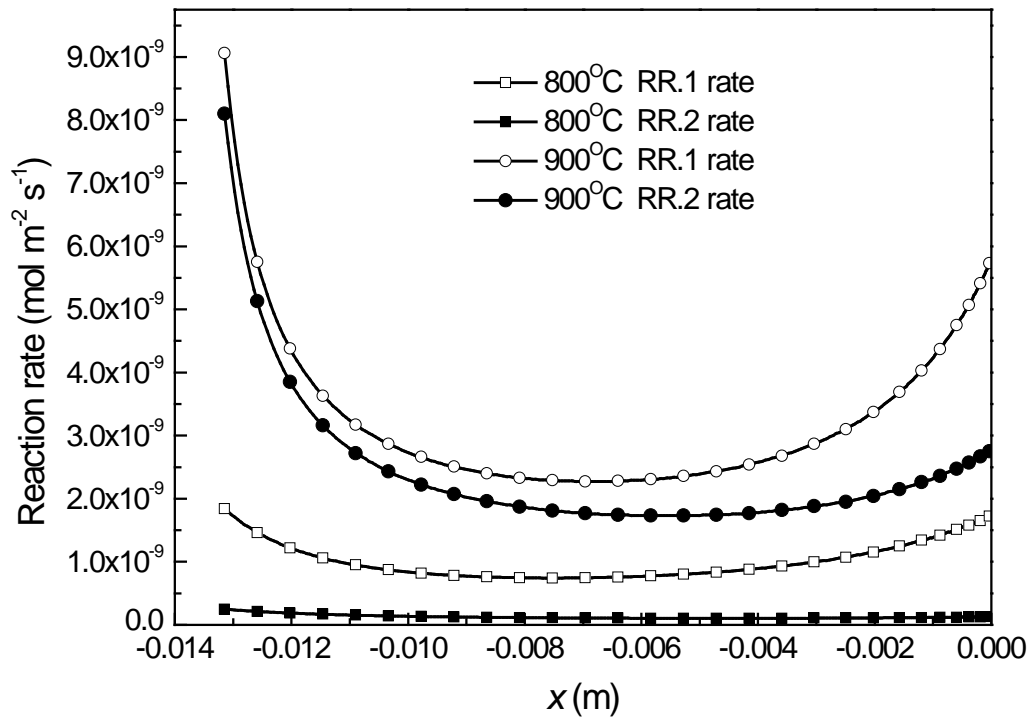
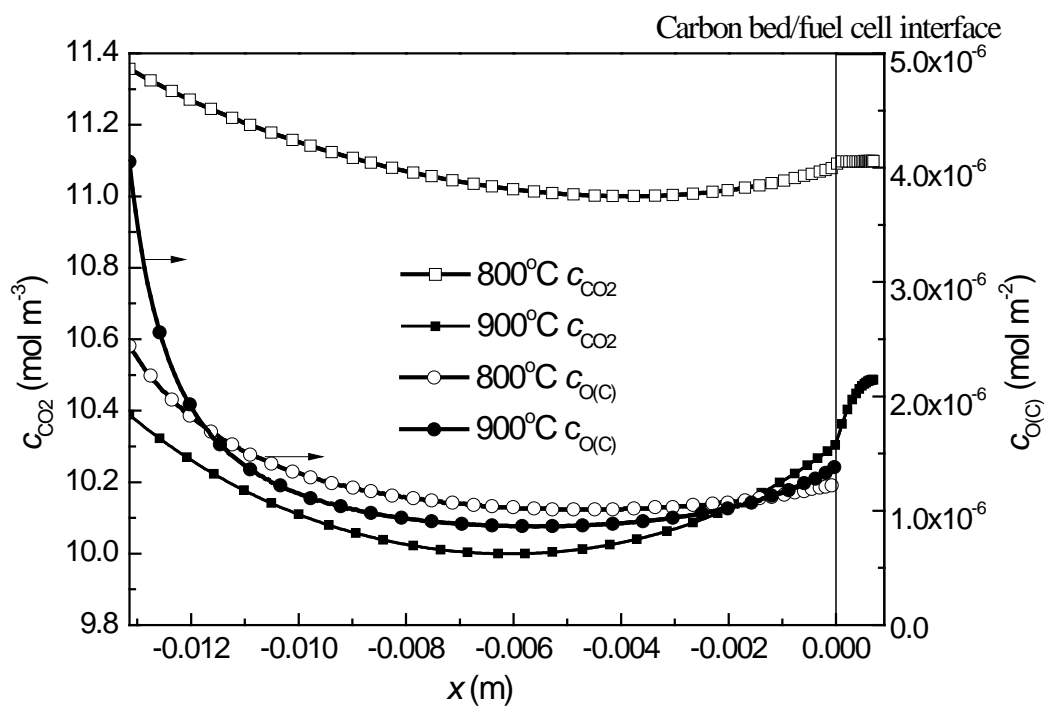


Fig.

12 Elementary reaction rates of RR.1 and RR.2 in carbon bed at 800°C and 900°C



**Fig.**

**13 Concentration distributions of CO<sub>2</sub> and adsorbed oxygen species O(C) at 800°C and 900°C**

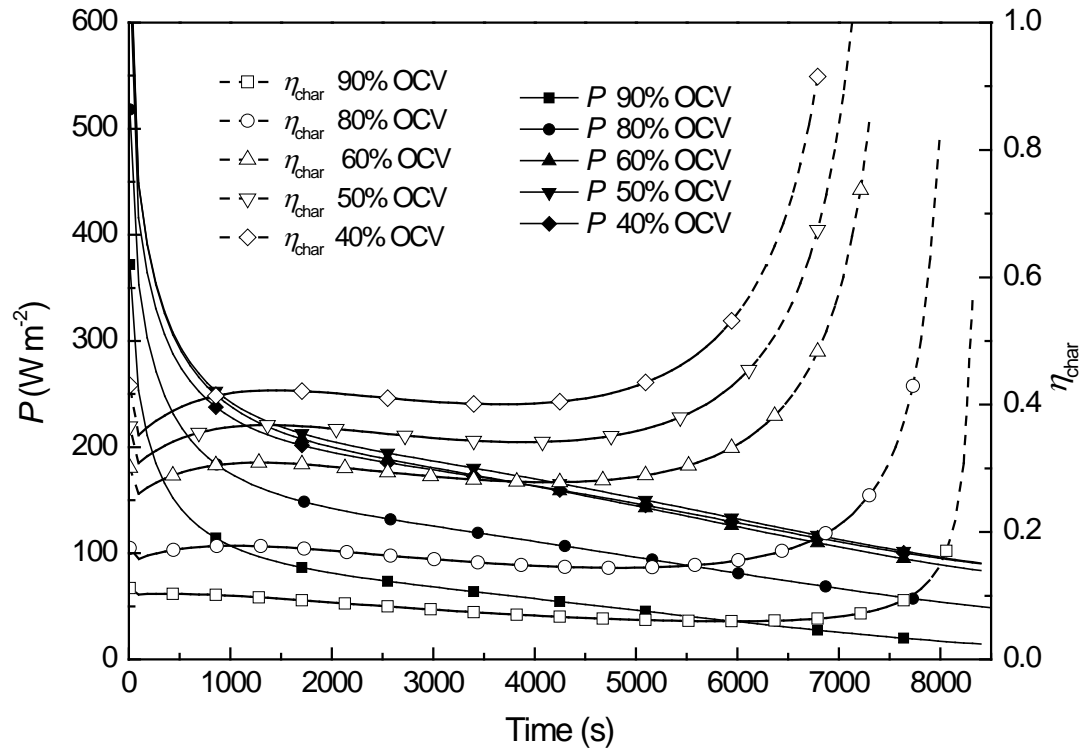


**Fig.**

**14 Power density  $P$  and carbon utilization  $\eta_{char}$  curves for different cell work voltages**

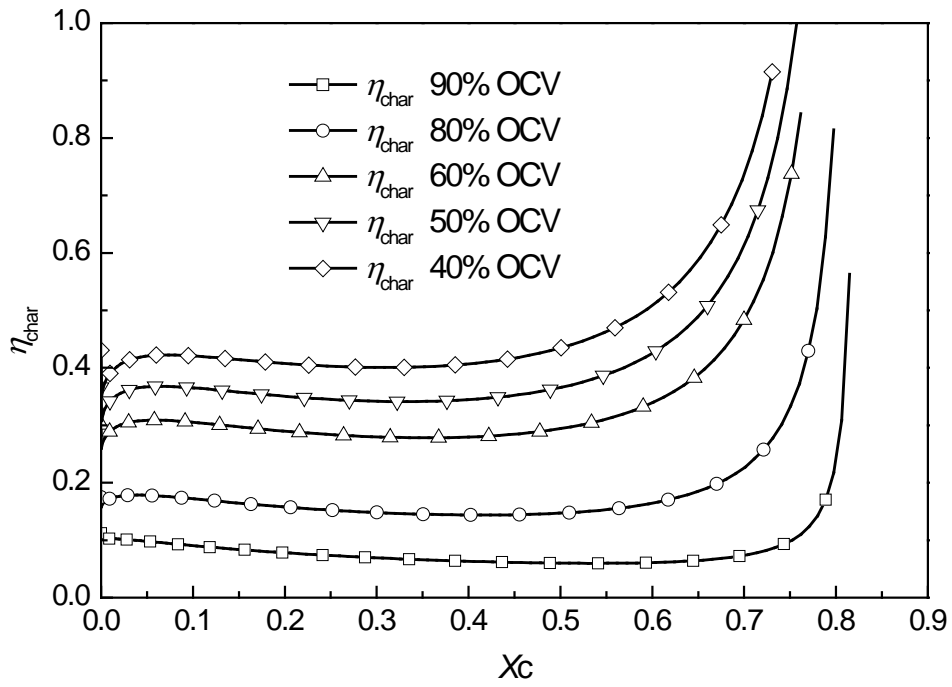


**Fig.**

**15 The relationship between carbon utilization  $\eta_{char}$  and conversion  $X_c$**

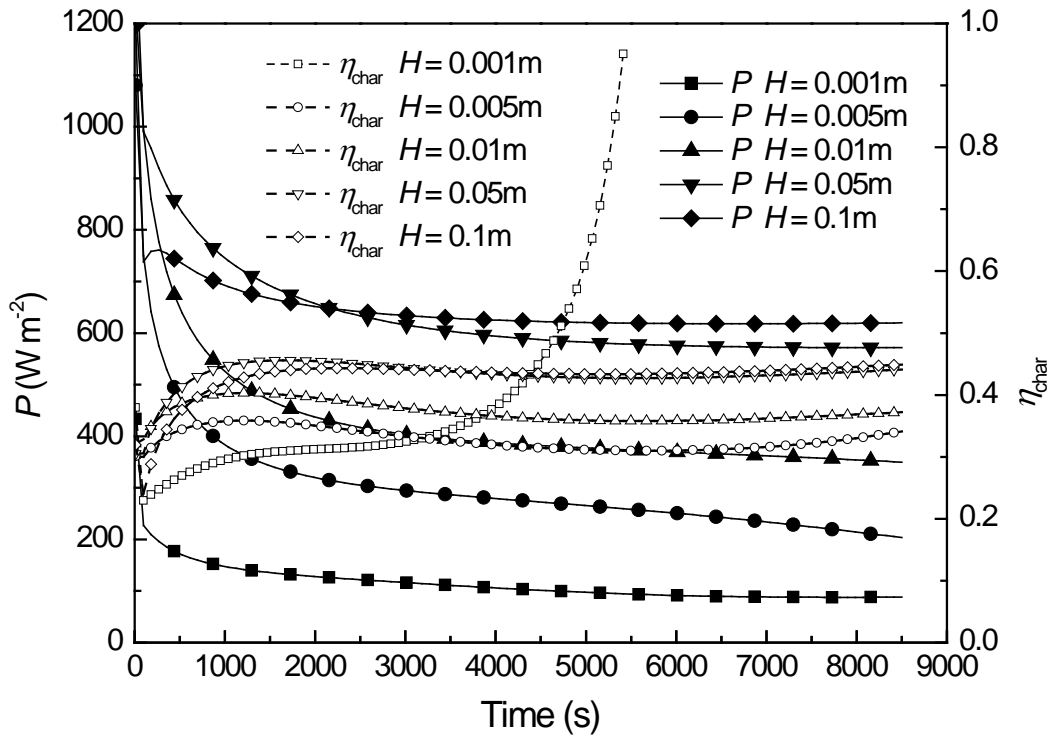


**Fig. 16 Power density and carbon utilization degree for different carbon bed heights**

## Nomenclature

$a_i$	pre-exponential factor in sticking coefficient expression
$A$	pre-exponential factor (in terms of cm, mol and s)
$b_i$	temperature exponent in sticking coefficient expression
$c$	concentration ( $\text{mol m}^{-3}$ )
$C_b$	bulk carbon atom
$C_{sites}$	surface carbon site concentration ( $\text{mol m}^{-2}$ )
$C_f$	free carbon site
$O(C)$	adsorbed oxygen atom species on carbon site
$CO(C)$	adsorbed carbon monoxide species on carbon site
$C_{dl}$	specific double-layer capacitance ( $\text{F m}^{-2}$ )
$d_i$	activation energy in sticking coefficient expression ( $\text{J mol}^{-1}$ )
$D$	diffusion coefficient ( $\text{m}^2 \text{s}^{-1}$ )
$E$	activation energy ( $\text{kJ mol}^{-1}$ )
$E_{ca}$	parameter in Eq. (37) ( $130 \text{ kJ mol}^{-1}$ )
$\eta_{a_{char}}$	carbon utilization degree
$F$	Faraday constant ( $96,485 \text{ C mol}^{-1}$ )
$i_0$	exchange current density ( $\text{A m}^{-2}$ )
$i_{surf}$	current density at the interface of carbon bed and cell anode
$I_F$	volumetric Faradaic current ( $\text{A m}^{-3}$ )
$j(s)$	species of j adsorbed on the surface of Ni
$k$	reaction rate constant (in terms of m, mol and s)
$K$	number of species
$M_j$	molecular weight ( $\text{kg mol}^{-1}$ )
$n$	temperature exponent fraction number of electronic or ionic conductor particles
$n_e$	number of electrons participating in the reaction
$n_t$	total number of particles per unit volume
$N$	number of the reactions
$P$	pressure (Pa)
$P$	whole range connection probabilities of same kinds of particles
$Q$	source term of charge balance equations ( $\text{A m}^{-3}$ )
$r_{el}$	mean radius of the electronic conductor particle (m)



$R$	gas constant ( $8.314 \text{ J mol}^{-1} \text{ K}^{-1}$ )
$R_{i,c}$	net rate of the removal of the carbon atoms from the bulk carbon ( $\text{kg m}^{-2} \text{ s}^{-1}$ )
$R_k$	source term of mass balance equations ( $\text{kg m}^{-3} \text{ s}^{-1}$ )
$\square$	
$s$	molar production rate ( $\text{mol m}^{-2} \text{ s}^{-1}$ )
$S^0$	initial sticking coefficient
$S^{eff}$	effective reaction area per unit volume ( $\text{m}^2 \text{ m}^{-3}$ )
$S_{gC}$	specific surface area of the activated carbon ( $\text{m}^2 \text{ kg}^{-1}$ )
$S_{gC,0}$	initial specific surface area of the activated carbon ( $\text{m}^2 \text{ kg}^{-1}$ )
$S_{Ni}$	Ni active surface area per unit volume ( $\text{m}^2 \text{ m}^{-3}$ )
$S_{STB}$	TPB active area per unit volume ( $\text{m}^2 \text{ m}^{-3}$ )
$u$	velocity of gaseous species ( $\text{m s}^{-1}$ )
$V_{bed}$	volume of carbon bed
$V_j, V_k$	diffusion volume
$W$	molecular weight of the gas-phase species in sticking coefficient reaction ( $\text{kg mol}^{-1}$ )
$x_c$	carbon conversion ratio
$x_k$	molar fraction of gas-phase species $k$
$Z$	coordination number

#### Greek letters

$\alpha$	transfer coefficient
$\beta$	tuning parameter ( $\Omega^{-1} \text{ m}^{-2}$ )
$\gamma$	parameter modeling the rate constant from sticking coefficient
$\Gamma$	surface sites density ( $\text{mol m}^{-2}$ )
$\varepsilon$	porosity
$\varepsilon_{ki}$	parameter modeling the species coverage
$\varepsilon_p$	carbon particle porosity
$\eta$	overpotential (V)
$\kappa$	permeability ( $\text{m s}^{-1}$ )
$\theta$	contact angle between the electronic and ionic conductors particles (rad)
$\theta_k$	surface coverage of species $k$
$\mu_{ki}$	parameter modeling the species coverage
$\nu$	stoichiometric coefficient

$\sigma$	conductivity ( $\text{S m}^{-1}$ )
$\tau$	tortuosity
$\lambda$	species symbol
$\psi$	structural parameter of carbonaceous fuel

#### Subscripts

ac	anode chamber
act	active layer
an	anode
ca	cathode
ec	electrochemical reactions
el	electronic conductor particles
elec	electronic
g	gas-phase species
$i$	reactions index
io	ionic conductor particles
ion	ionic
$k$	species index
Kn	Knudsen
OCV	open circuit voltage
ref	reference
s	surface species
sp	support layer

#### Superscripts

0	parameter at equilibrium conditions
bulk	bulk phase
eff	effective
TPB	three-phase boundary

**Table 1** Reduced heterogeneous reaction mechanism for carbon gasification and mechanism on the Ni-based catalysts

<b>Carbon gasification mechanism</b>				
Elementary reactions		A <sup>a</sup>	$\sigma^b$ (kJ mol <sup>-1</sup> )	E <sup>a</sup> (kJ mol <sup>-1</sup> )
RR.1f	$\text{CO}_2 + \text{C}_f \rightleftharpoons \text{CO} + \text{O}(\text{C})$	5e-3	--	185e3
RR.1r		108	--	89.7e3
RR.2	$\text{C}_b + \text{O}(\text{C}) \longrightarrow \text{CO} + \text{C}_f$	1e13	28e3	375e3
RR.3	$\text{C}_b + \text{CO}_2 + \text{O}(\text{C}) \longrightarrow 2\text{CO} + \text{O}(\text{C})$	1e-4	--	58e3
RR.4f	$\text{C}_f + \text{CO} \rightleftharpoons \text{CO}(\text{C})$	0.89	--	148e3
RR.4r		1e13	53e3	455e3
RR.5	$\text{CO} + \text{CO}(\text{C}) \longrightarrow \text{CO}_2 + 2\text{C}_f$	1.01e7	--	262e3
<b>The heterogeneous reaction mechanism on the Ni-based catalysts</b>				
Adsorption and desorption reactions		A <sup>c</sup> (cm, mol, s)	n <sup>c</sup>	E <sup>c</sup> (kJ mol <sup>-1</sup> )
R.1f	$\text{O}_2 + \text{Ni}(\text{s}) \rightleftharpoons \text{O}(\text{s}) + \text{O}(\text{s})$	1e-2	--	0
R.1r		4.283e23	--	474.95
R.2f	$\text{CO}_2 + \text{Ni}(\text{s}) \rightleftharpoons \text{CO}_2(\text{s})$	1e-5	--	0
R.2r		6.447e7	--	25.98
R.3f	$\text{CO} + \text{Ni}(\text{s}) \rightleftharpoons \text{CO}(\text{s})$	5e-1	--	0
R.3r		3.563e11	--	111.27
		$\theta_{\text{CO}(\text{s})}^d$		-50.0
<b>Surface reactions</b>				
R.4f		5.2e23	--	148.10
R.4r	$\text{C}(\text{s}) + \text{O}(\text{s}) \rightleftharpoons \text{CO}(\text{s}) + \text{Ni}(\text{s})$	1.354e22	-3	116.12
		$\theta_{\text{CO}(\text{s})}^d$		-50.0
R.5f	$\text{CO}(\text{s}) + \text{O}(\text{s}) \rightleftharpoons \text{CO}_2(\text{s}) + \text{Ni}(\text{s})$	2e19	--	123.6
		$\theta_{\text{CO}(\text{s})}^d$		-50.0
R.5r		4.563e23	-1	89.32

<sup>a</sup> Arrhenius parameters for the rate constants are written in the form:  $k = A \exp(-E / RT)$

<sup>b</sup> For k2 and k4r, the activated energy is fit to the normal distribution because the activated energy for species in the two reactions is not the same all through the carbon surface sites:

$$k = \int_0^{+\infty} A \exp\left(-\frac{E}{RT}\right) \frac{1}{\sqrt{2\pi}\sigma} \exp\left(-\frac{(E - E_a)^2}{2\sigma^2}\right) dE$$

<sup>c</sup> Arrhenius parameters for the rate constants are written in the form:  $k = ATn \exp(-E / RT)$

<sup>d</sup> Coverage-dependent activation energy

**Table 2 Summary of model equations for different processes in SO-DCFCs**

Processes	Model equations
<b>Anode Ni/YSZ electrode heterogeneous chemistry</b>	
Gaseous adsorption-desorption reactions	$\sum_{k=1}^{K_g+K_s} v'_k \chi_k \rightleftharpoons \sum_{k=1}^{K_g+K_s} v''_k \chi_k \quad (14)$
Net molar production rates	$\dot{s}_k = \sum_{i=1}^N (v''_{ki} - v'_{ki}) k_i \prod_{k=1}^{K_g+K_s} c_k^{v'_{ki}} \quad (15)$
Rate constant	$k_i = A_i T^{n_i} \exp\left(-\frac{E_i}{RT}\right) \prod_{k=1}^{K_g+K_s} \theta_k^{\mu_{ki}} \exp\left(-\frac{\varepsilon_{ki} \theta_k}{RT}\right) \quad (16)$
Rate constant of adsorption reactions	$k_i = \frac{S_i^0}{\Gamma^\gamma} \sqrt{\frac{RT}{2\pi W}} \quad (17)$
	$\gamma = \sum_k^{K_s} v'_{ki} \quad (18)$
	$S_i^0 = a_i T^{b_i} \exp\left(-\frac{d_i}{RT}\right) \quad (19)$
<b>Electrode electrochemistry</b>	
Current source	$Q_{an} = i_{0,ca} L_{TPB} \quad (20)$
Length-specific current density	$i_{0,an} = 2F(k_{ct,f} c_{(YSZ)} c_{CO_2(Ni)} - k_{ct,b} c_{CO(Ni)} c_{O^{2-}(YSZ)}) \quad (21)$
Charge transfer reaction rate constants	$k_{ct,f} = k_{ct,f}^0 \exp\left(-\left(1-\alpha\right) \frac{n_e F}{RT} \eta_{an}\right) \quad (22)$
	$k_{ct,b} = k_{ct,b}^0 \exp\left(\frac{\alpha n_e F}{RT} \eta_{an}\right) \quad (23)$
Anode electrode overpotential	$\eta_{an} = V_{elec,an} - V_{ion,an} - V_{ref,an} \quad (24)$
	$k_{ct,f}^0 = \frac{i_{0,CO_2}}{2FL_{TPB} c_{(YSZ)}^0 c_{CO_2(Ni)}^0} \quad (25)$
	$k_{ct,b}^0 = \frac{i_{0,CO_2}}{2FL_{TPB} c_{CO(Ni)}^0 c_{O^{2-}(YSZ)}^0} \quad (26)$
Exchange current density	$i_{0,CO_2} = k_{CO_2} \exp\left(-\frac{\Delta G_{CO_2}}{RT}\right) \quad (27)$
<b>Charge balance</b>	
Electrode charge balance equations	$\nabla(-\sigma^{eff} \nabla V_i) = Q \quad (28)$
Ionic charge at the cathode electrode	$\nabla[-\sigma_{ion,pos}^{eff} \nabla V_{ion,pos}] = Q_{ion,pos} \quad (29)$
	$= -i_{0,ca} S_{TPB,ca} \left\{ \frac{c_{O_2}^{TPB}}{c_{O_2}^{bulk}} \exp\left[\frac{\alpha n_e F \eta_{ca}}{RT}\right] - \exp\left[-\frac{(1-\alpha) n_e F \eta_{ca}}{RT}\right] \right\} \quad (30)$
Electronic charge at the cathode electrode	$\nabla[-\sigma_{elec,ca}^{eff} \nabla V_{elec,ca}] = Q_{elec,ca} = -Q_{ion,ca} \quad (31)$
Ionic charge at the anode electrode	$\nabla[-\sigma_{ion,an}^{eff} \nabla V_{ion,an}] = Q_{ion,pos} = Q_{an} \quad (32)$

Electronic charge at the anode electrode  $\nabla \cdot (-\sigma_{elec,an} \nabla V_{elec,an}) = Q_{elec,an} = -Q_{an}$  (33)

Ionic charge at the electrolyte  $\nabla \cdot (-\sigma_{ion,electrolyte}^{eff} \nabla V_{ion,electrolyte}) = 0$  (34)

Cathode local overpotential  $\eta_{ca} = V_{elec,ca} - V_{ion,ca} - V_{ref,ca}$  (35)

Open circuit voltage (OCV)  $V_{OCV} = \frac{RT}{n_e F} \ln \left( \frac{p_{ca}^{O_2}}{p_{an}^{O_2}} \right)$  (36)

Cathode exchange current density  $i_{0,ca} = \frac{\beta RT}{4F} \exp \left( -\frac{E_{ca}}{RT} \right) (p_{ca}^{O_2})^{0.25}$  (37)

### Mass balance

Mass balance in a porous electrode  $\varepsilon \frac{\partial c_{k,g}}{\partial t} + \nabla \cdot (-D_k^{eff} \nabla c_{k,g}) = R_{k,g}$  (38)

$$D_k^{eff} = \left( \frac{1}{D_{k,mole}^{eff}} + \frac{1}{D_{k,Kn}^{eff}} \right)^{-1} \quad (39)$$

Cathode Faraday's law  $R_{O_2} = \frac{Q_{elec,ca}}{4F}$  (40)

Gaseous and surface species  $R_k = S^{eff} \cdot \dot{s}_k = S^{eff} \cdot \sum_{i=1}^{N+2} (v_{ki}'' - v_{ki}') k_i \prod_{k=1}^{K_g + K_s + 2} c_k^{v_{ki}'} \quad (41)$

---

**Table 3 Boundary conditions**

Boundary	Ionic charge	Electronic charge	Mass balance	Momentum balance
B.C 1 <sup>a</sup>	—	—	$c_{gas\_in}$	Pressure $P_0$
B.C 2	Insulation	0	Continuity for gaseous species	Inward flux $q_{in}$ /Insulation for surface species
B.C 3	Continuity	Continuity	Continuity	Continuity
B.C 4	Continuity	Insulation	Insulation	Insulation
B.C 5	Continuity	Insulation	Insulation	Insulation
B.C 6	Insulation	$V_{ca}$	$c_{gas\_ca}$	Pressure $P_0$

<sup>a</sup> model geometric boundaries are labeled in Fig. 3

**Table 4 Pore structure parameters in porous electrode**

<b>Cell layer</b>	<b>Porosity</b>	<b>Mean pore diameter(<math>\mu\text{m}</math>)</b>	<b><math>S_{\text{TPB}}(\text{m}^2 \text{ m}^{-3})</math></b>	<b><math>L_{\text{TPB}}(\text{m m}^{-3})</math></b>	<b><math>S_{\text{Ni}}(\text{m}^2 \text{ m}^{-3})</math></b>
Anode support layer	0.335	0.193	2.22e5	2.76e7	3.97e6
Anode active layer	0.335	0.129	3.33e5	6.20e7	5.96e6
Cathode layer	0.335	0.161	2.66e5	3.97e7	--

**Table 5 Properties and parameters for model calculation**

Property and parameter	Value or expression	Unit
Ionic conductivity ( $\sigma_{ion}$ )		
ScSZ	$6.92E4\exp(-9681/T)$	$S\ m^{-1}$
YSZ	$3.34E4\exp(-10300/T)$	$S\ m^{-1}$
Electronic conductivity ( $\sigma_{ele}$ )		
LSM	$4.2E7/T\exp(-1150/T)$	$S\ m^{-1}$
Ni	$3.27E6-1065.3T$	$S\ m^{-1}$
Equivalent ionic conductivity of electrolyte layer ( $\sigma_{electrolyte}$ )	$-3.622E-5T^2+0.083T-46.343^a$	$S\ m^{-1}$
Concentration of oxygen interstitial in the YSZ ( $c_{O^{2-}(YSZ)}$ )	4.45E4	$mol\ m^{-2}$
Concentration of oxygen vacancy in the YSZ ( $c_{(YSZ)}$ )	4.65E3	$mol\ m^{-2}$
Maximum surface sites density ( $\Gamma$ )	2.6E-5	$mol\ m^{-2}$
Cathode tortuosity ( $\tau_{ca}$ )	3.0	—
Ni felt current collector porosity	0.6 <sup>b</sup>	—

<sup>a</sup> Experimentally measured<sup>b</sup> As received